Mat. Res. Soc. Symp. Proc. Vol. 701 © 2002 Materials Research Society

Convection Effects in Three-Dimensional Dendritic Growth

Yili Lu[1], C. Beckermann[1], and A. Karma[2]
[1]Department of Mechanical and Industrial Engineering, University of Iowa, Iowa City, IA 52242-1527, U.S.A.
[2]Department of Physics and Center for Interdisciplinary Research on Complex Systems, Northeastern University, Boston, MA 02115, U.S.A.

ABSTRACT

A phase-field model is developed to simulate free dendritic growth coupled with fluid flow for a pure material in three dimensions. The preliminary results presented here illustrate the strong influence of convection on the three-dimensional (3D) dendrite growth morphology. The knowledge of the flow and temperature fields in the melt from the simulations allows for a detailed understanding of the convection effects on dendritic growth.

INTRODUCTION

Dendrites are the most common microstructure found in engineering materials. The shape, size and orientation of the dendrites determine to a large extent the physical and chemical properties of cast and welded metals. While numerous experimental, numerical and analytical studies have been performed to understand dendritic growth from the melt in diffusion-controlled situations [1-10], the pattern selection and microstructure evolution are not well understood for convection-controlled growth. Convection in the melt during solidification can be caused by buoyancy forces, dendrite movement, shrinkage, or a variety of imposed flows.

In the past ten years, the phase-field method [11-14] has become a popular computational tool to simulate microstructure formation in solidification. The main advantage of the phase-field method is that it avoids direct tracking of the sharp solid-liquid interfaces [15-17]. Based on an analysis of the thin interface limit, Karma and Rappel [18] proposed a computationally efficient phase-field method that allows for quantitative modeling of dendritic crystal growth. Beckermann et al. [19] employed the phase-field method to study convective effects on dendritic growth in two dimensions (2D). The numerical results show that convection can significantly alter the operating state of a dendrite tip and dendritic sidebranching. Very recently, Jeong et al. [20] investigated the effect of fluid flow on 3D dendritic growth using an adaptive-grid finite element method. They found that the flow and dendrite growth shapes in three dimensions are very different from those in two dimensions.

In this paper, our previous simulations of 2D dendritic growth with convection [19] are extended to three dimensions. Preliminary results are presented that illustrate the effects of convection on dendritic growth.

GOVERNING EQUATIONS

The governing equations for flow and heat transfer are the same as those derived in Ref. [19], while the phase-field equation is taken from the work of Karma and Rappel [18]. The effects of flow in the phase-field equation are neglected. All equations are valid in the single-phase solid and liquid regions as well as in the diffuse interface region, where the phase-field variable, ψ,

varies from –1 to +1. An auxiliary variable, the solid fraction ε_s, is introduced as $\varepsilon_s = (1+\psi)/2$. The equations can be summarized as follows.

Mass conservation:

$$\nabla \cdot \left[(1-\varepsilon_s)\cdot \bar{v}_l\right] = 0, \tag{1}$$

where $\bar{v}_l$ is the intrinsic velocity of the liquid.

Momentum conservation:

$$\begin{aligned} &\frac{\partial}{\partial t}\left[(1-\varepsilon_s)\bar{v}_l\right] + \nabla\cdot\left[(1-\varepsilon_s)\bar{v}_l\bar{v}_l\right] = -(1-\varepsilon_s)\nabla p \\ &+ \nu_l\nabla^2\left[(1-\varepsilon_s)\bar{v}_l\right] - \nu_l\frac{h\varepsilon_s^2(1-\varepsilon_s)}{W_o^2}\bar{v}_l, \end{aligned} \tag{2}$$

where ν_l, p, and t are the kinematic viscosity, pressure, and time, respectively. The parameter W_0 is representative of the interface thickness (see below). The last term on the right-hand side of equation (2) is a distributed interfacial force that forces the liquid velocity to vanish across the diffuse interface as the solid is approached. The coefficient h is a constant equal to 5.514, which was determined from an asymptotic analysis that forces the velocity profile to approach that for a no-slip condition at a sharp interface located at $\varepsilon_s = 0.5$.

Energy conservation:

$$\frac{\partial u}{\partial t} + \nabla\cdot\left[(1-\varepsilon_s)\bar{v}_l u\right] = D\nabla^2 u + \frac{\partial \varepsilon_s}{\partial t}, \tag{3}$$

where D is the thermal diffusivity. The dimensionless temperature u is defined as $u = (T - T_M)/(L/c_p)$, where T_M, L, and c_p are the melting temperature, latent heat, and specific heat at constant pressure, respectively.

Phase-field equation:

$$\tau(\mathbf{n})\frac{\partial\psi}{\partial t} = \left[\psi - \lambda u(1-\psi^2)\right](1-\psi^2) + \nabla\cdot\left[W^2(\mathbf{n})\nabla\psi\right] + \sum_{\xi=x,y,z}\frac{\partial}{\partial\xi}\left[|\nabla\psi|^2 W(\mathbf{n})\frac{\partial W(\mathbf{n})}{\partial(\partial_\xi\psi)}\right], \tag{4}$$

where λ is a dimensionless parameter that controls the strength of the coupling between the phase and temperature fields, and **n** is the interface normal. The interface thickness function W depends on the orientation of the interface and is given by $W(\mathbf{n}) = W_0 a_s(\mathbf{n})$. In the limit of vanishing interface kinetics, $\tau(\mathbf{n})$ is chosen as $\tau(\mathbf{n}) = \tau_0 a_s^2(\mathbf{n})$, with

$$a_s(\mathbf{n}) = (1-3\varepsilon_4)\left[1+\frac{4\varepsilon_4}{1-3\varepsilon_4}\frac{(\partial_x\psi)^4+(\partial_y\psi)^4+(\partial_z\psi)^4}{(\nabla\psi)^4}\right], \quad (5)$$

where ε_4 is the anisotropy strength. All other details can be found in the original references [18, 19].

NUMERICAL METHOD

The energy and phase-field equations are solved using an explicit finite difference method on uniform grids that are different from each other. The node spacing for the energy equation is exactly twice as large as the one for the phase-field equation, as illustrated in figure 1. This can be done without loss of accuracy, because the thermal diffusion length is much larger than the diffuse interface thickness. The temperatures on the fine-mesh nodes for use in the phase-field equation are obtained by linear interpolation. Extensive numerical tests were performed to validate this approach for the ranges of the governing parameters considered here.

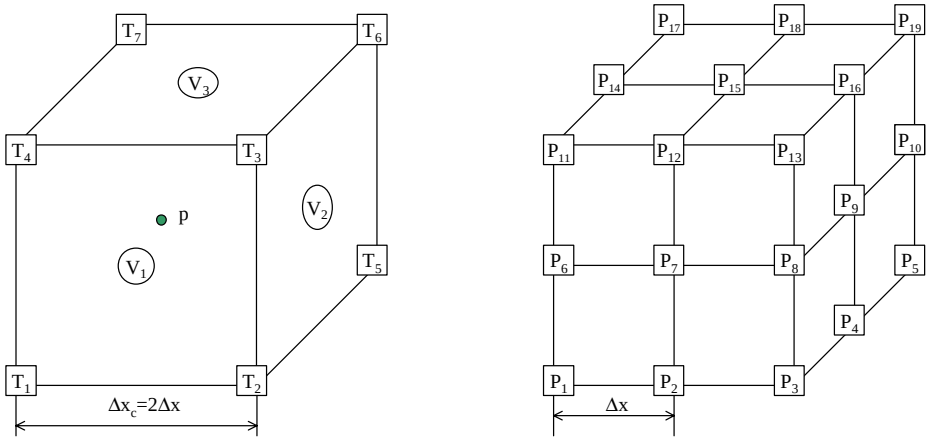

Figure 1. Illustration of (a) the coarse grids used or the solution of the energy and flow equations and (b) the fine grid for the phase-field equation. The temperatures nodes are located on the eight corners of the cube in figure 1a, the velocity nodes are located on the centers of the six surfaces of the cube in figure 1a, the pressure node is located in the center of the cube in figure 1a, and the phase-field nodes are located on every corner of the small cubes in figures 1b.

The mass and momentum equations are solved using a modified version of the finite element CFD code FEAST [21]. This code was originally developed by Turek and coworkers in the Department of Mathematics at the University of Dortmund, Germany. Descriptions of the discretization technique, the error control method, and the multi-grid solution scheme can be found online [21]. The code was modified to accommodate the non-standard forms of the mass and momentum equations, Eqs. (1) and (2). As shown in figure 1a, the velocity is defined at the

center of the six surfaces of the element, while the pressure is defined at the center of the volume element. Most importantly, the element edge length is again twice as large as the node spacing used in the solution of the phase-field equation. Since most of the total computational effort is associated with the solution of the flow equations, this method offers tremendous savings in both computer time and memory. It was verified through extensive numerical tests that the use of a coarser mesh for the flow equations does not sacrifice accuracy for the cases considered here. The velocities were interpolated to the appropriate locations for use in the solution of the energy equation. The flow equations are solved in a fully implicit manner. As found previously by the present authors [19], this allows for the use of a larger time step (about five times as large) for the flow equations than for the phase-field and energy equations; however, this procedure was not yet utilized in the present study.

Numerous benchmark problems were solved using the present 3D code in order to validate the numerical method. Only one of these, flow around an infinitely long circular cylinder at low Reynolds numbers, is described here. The cylinder was represented by a (stationary) distribution of the phase field variable, which varies in a hyperbolic tangent fashion across the cylinder-fluid interface. In other words, the cylinder was not explicitly discretized. For the present simulations at low Reynolds numbers, the computational domain has to be much larger than the cylinder so that the flow field is not influenced by the boundaries [22]; hence, a non-uniform grid of hexahedral elements was utilized. A two-dimensional cut of the mesh is plotted in figure 2a. Since the elements are densely concentrated at the center of the cut where the cylinder is present, an enlarged view of this region of the mesh is shown in figure 2b. The flow is from left (x=0 plane) to right (x=10 plane) in this figure. A uniform inlet velocity and a zero-velocity gradient at the outlet are used as boundary conditions on these two planes. Slip boundary conditions are applied at the bottom (y=0 plane) and top (y=10 plane) boundaries. Two-dimensional results for an infinitely long cylinder are desired for the comparison with the benchmark results. Hence, slip boundary conditions are applied on the front and back boundaries. Then, the size of the domain in the z-direction (parallel to the axis of the cylinder) is arbitrary.

Using the computed flow results, the drag coefficient, C_D, of the cylinder was determined as a function of the Reynolds number. A comparison of the present results for the drag coefficient with previous experimental measurements [23, 24] is shown in figure 3. The agreement is good for all Reynolds numbers.

RESULTS

Figure 4 shows the physical domain and conditions used in the present simulation of free dendritic growth in the presence of melt convection. A spherical seed at the melting temperature (u=0) is located in the center of a cubic domain of volume 204.8^3. The [100], [010], and [001] crystalline directions are aligned with the x, y, and z coordinates, respectively. Undercooled melt enters the domain at the x=0 plane with a uniform velocity of U=1 and dimensionless temperature of $u_{in}=\Delta=-0.55$. The melt exits at the opposing end of the domain. Symmetry or slip boundary conditions are imposed on the four planes normal to the inlet and outlet. For the present low Reynolds number flow, symmetry allows the computations to be performed in only a quarter of the domain. Other conditions include D=4, $\varepsilon_4 = 0.05$, and $\mathrm{Pr} = \nu / D = 2.5$. The calculations were performed on a uniform grid of 128x64x64 nodes for the flow and temperature fields and of 256x128x128 nodes for the phase field.

Figure 5 shows computed dendrite shapes at various times. Since the dendrite would be completely symmetric in the absence of flow, it is obvious that the convection dramatically alters the growth morphology. The arms growing into the flow, in the upstream direction, grow much faster than the cross-stream arms. The arm pointing in the downstream direction grows so slowly that it is virtually non-existent.

The flow field is illustrated in Figures 6 to 8. Figure 6 shows the general characteristic of the streamlines around the dendrite. Figures 7 and 8 show representative streamlines on the upstream and downstream sides of the dendrite, respectively. The flow advects heat from the upstream to the downstream side. Consequently, the temperature field around the dendrite is very asymmetrical, as shown in figure 9. The temperature gradients are largest at the upstream tip, resulting in the large growth velocities there. The temperature in the wake of the dendrite is more uniform and closer to the melting point. Compared to the downstream arm, the cross-stream arms suffer much less from the convective transport of heat. This can be seen from the streamlines in figures 6 to 8. Most of the fluid that passes near the upstream dendrite arm and gets heated, flows through the space between the four cross-stream arms. The melt that passes directly by the cross-stream arm tips originates primarily from the far field and is not heated by any upstream structure. As can be seen from figure 6, the shape of the cross-stream arms is very asymmetrical in the z plane, which again is caused by advection of heat around those arms.

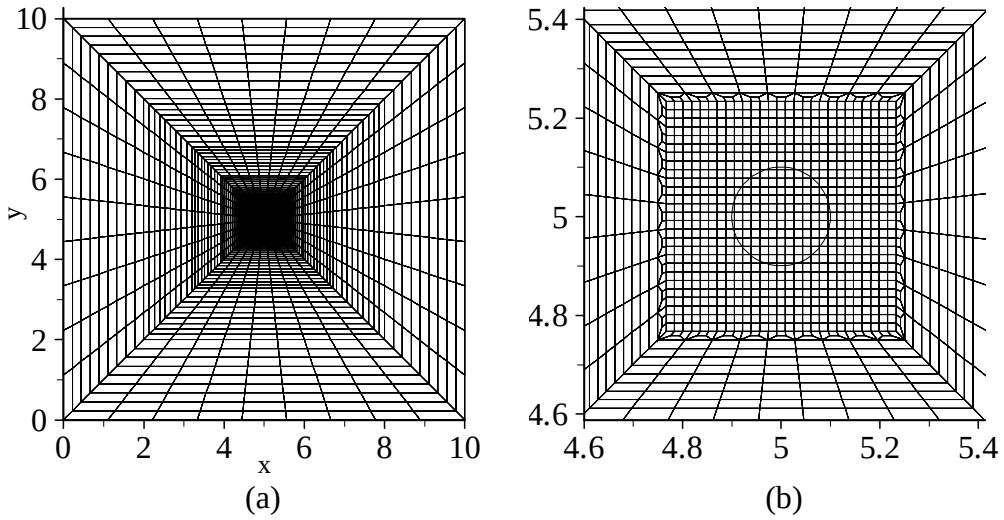

Figure 2. Two-dimensional x-y cut of the non-uniform mesh used for solving the benchmark problem of low Reynolds number flow around a circular cylinder. The cylinder axis is in the z-direction, and the mesh in the z-direction is a simple extension of the cut shown above. The domain size is 10x10x0.8. (a) Complete view of the mesh in two dimensions. (b) Enlarged view of the mesh in the center region of the domain. The circle represents the cylinder in this 2D cut. The cylinder is defined by a (stationary) distribution of the phase-field variable, with a hyperbolic tangent variation across the cylinder-fluid interface (not shown).

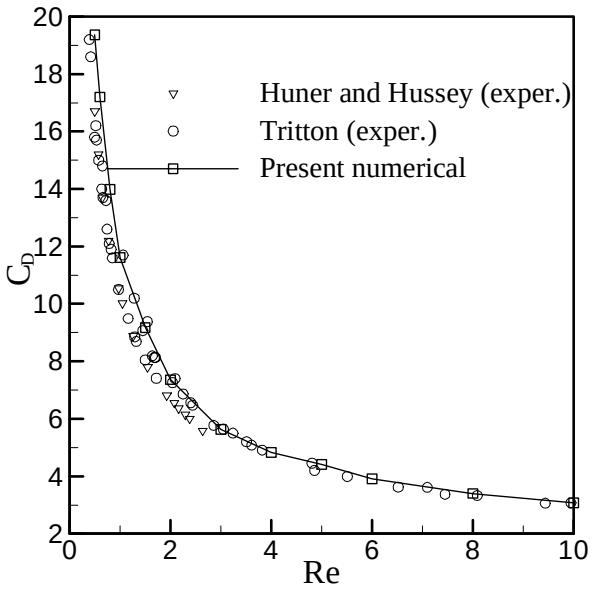

Figure 3. Comparison of measured [23, 24] and predicted drag coefficients as a function of Reynolds number for flow around an infinitely long circular cylinder.

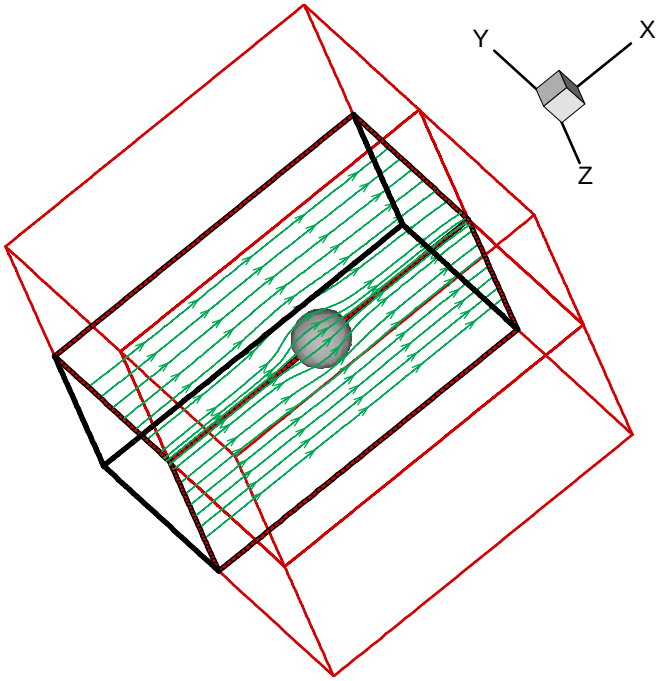

Figure 4. Physical (large box defined by red lines) and computational (small box defined by thick black lines) domains used in the present simulation of free dendritic growth into an undercooled melt in the presence of a forced flow (indicted by green streamlines). The size of the physical domain is 204.8^3. The seed is a sphere located in the center of the physical domain.

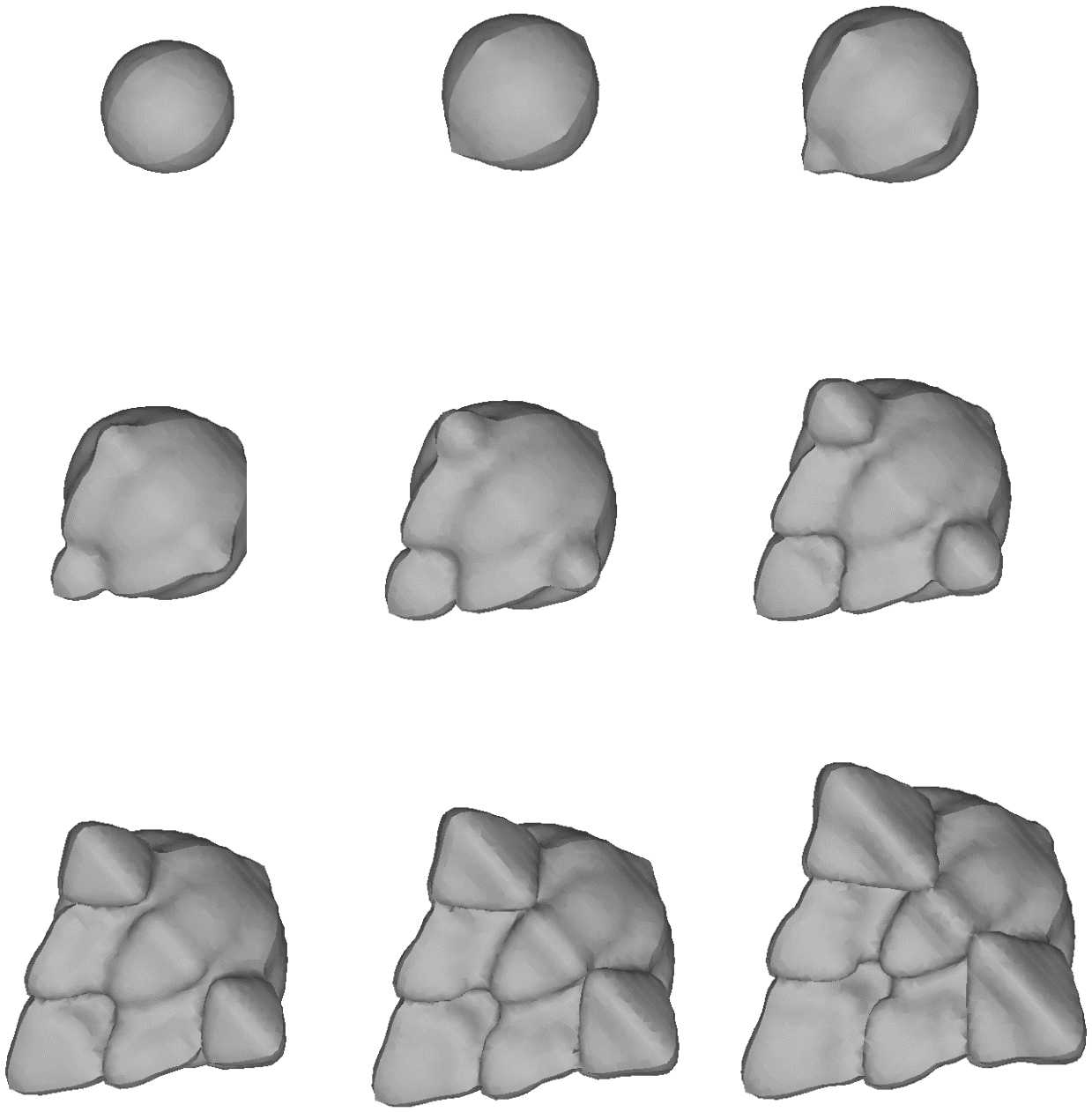

Figure 5. Snapshots of the evolving dendrite structure under the influence of convection convection. The dimensionless time interval between the snapshots is $\Delta t/\tau_0 = 8$. The input parameters are $\Delta = -0.55$, $D = 4$, $\varepsilon_4 = 0.05$, $Pr = \nu / D = 2.5$, $U = 1$, and $\lambda = 6.383$.

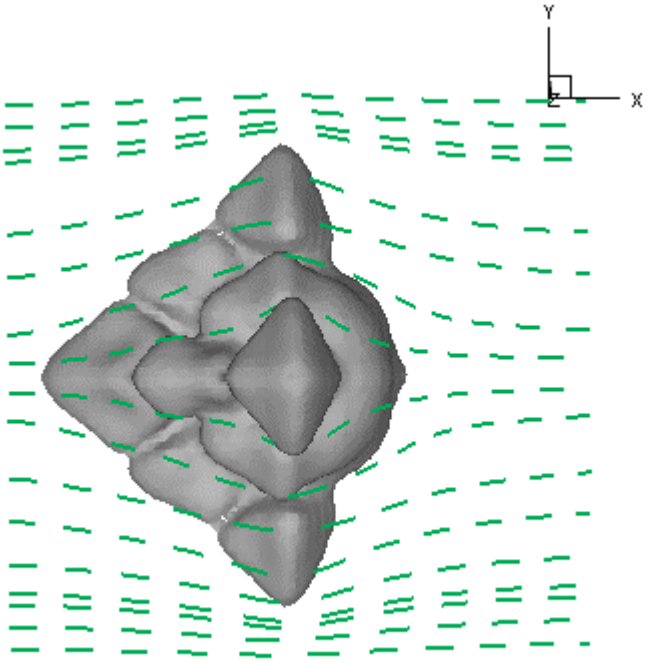

Figure 6. Streamlines around the dendrite viewed in the z-direction.

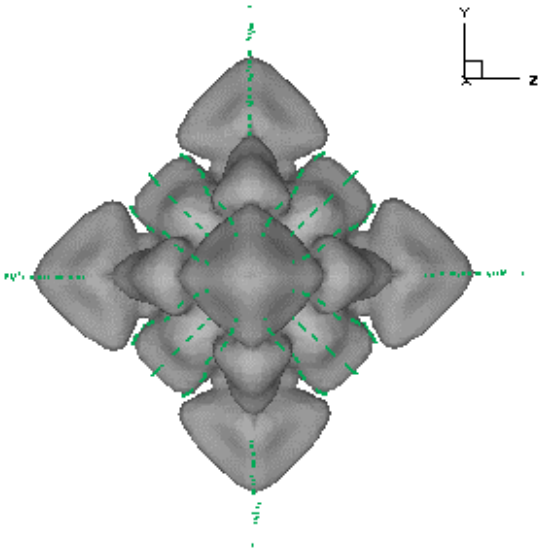

Figure 7. Streamlines on the upstream side viewed from the negative x-direction.

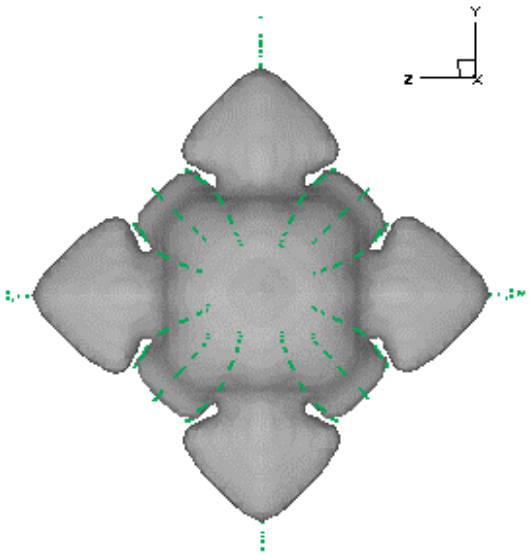

Figure 8. Streamlines on the downstream side viewed from the positive x-direction.

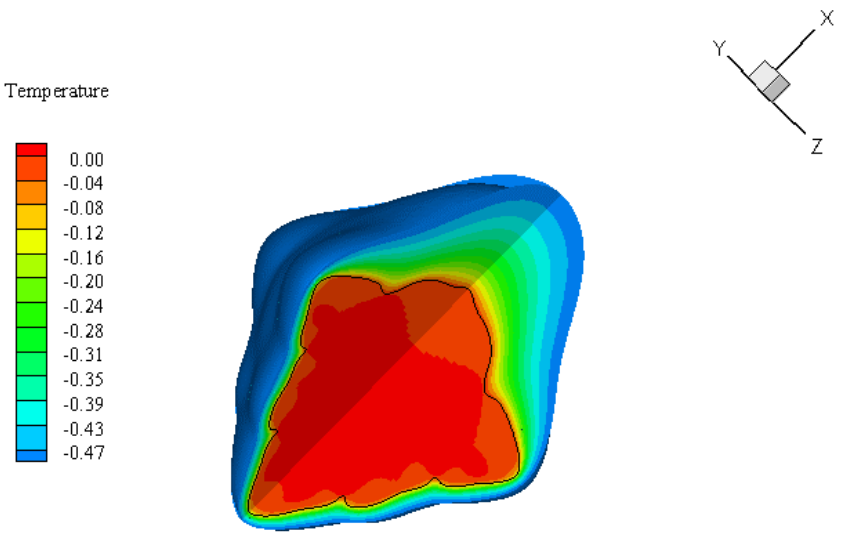

(a)

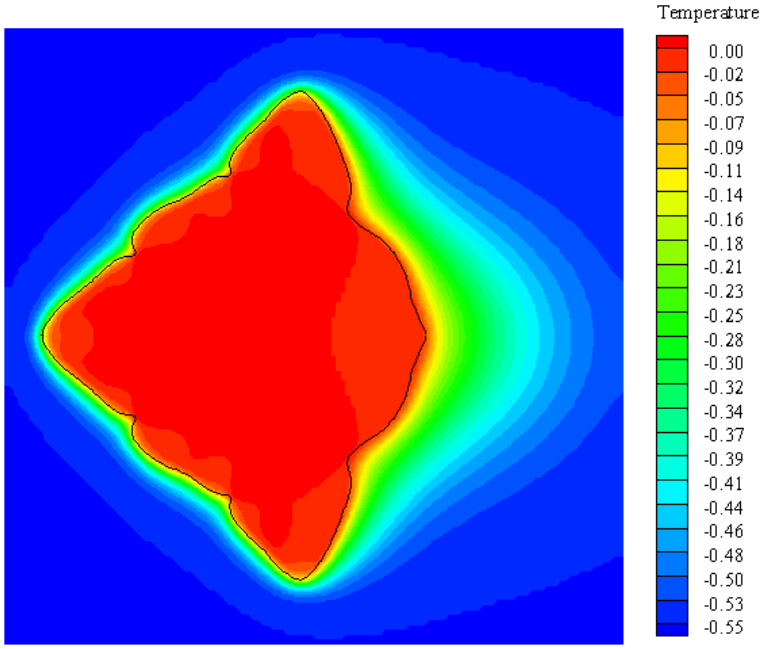

(b)

Figure 9. Temperature fields around the dendrite. The black line represents the interface contour. (a) 3D view of the temperatures (for clarity, the first octant is cut away and temperatures below -0.47 are not shown). (b) 2D cut of the temperature field at the y=0 plane.

CONCLUSIONS

A phase-field method has been developed to simulate free dendritic growth into an undercooled melt in three dimensions in the presence of a forced flow. Convection is found to significantly alter the growth morphology of the dendrite simulated. While the flow and temperature results presented here allow for a qualitative understanding of the effects of convection, a comparison of the predictions with relevant dendrite growth theories and experimental results is still underway.

ACKNOWLEDGEMENTS

This research was supported by NASA under Contract No. NCC8-94. The authors wish to thank Prof. Turek for his help with the FEAST code.

REFERENCES

1. W. A. Tiller, K. A. Jackson, J. W. Rutter and B. Chalmers, Acta Metall. **1**, 428(1953).
2. W. W. Mullins and R. F. Sekerka, J. Appl. Phys. **34**, 323 (1963); **35**, 444 (1964).
3. M. E. Glicksman, R. J. Schaefer and J. D. Ayers, Metall. Trans. A **7**, 1747 (1976).
4. M. E. Glicksman and N. B. Singh, J. Cryst. Growth **98**, 277 (1989).
5. R. Trivedi, Acta. Metall. **18**, 287 (1970); J. Cryst. Growth **49**, 1037 (1980).
6. G. B. McFadden, A. A. Wheeler, R. J. Braun, S. R. Coriell and R. F. Sekerka, Phys. Rev. E **48**, 2016 (1993).
7. W. Oldfield, Mater. Sci. Eng. **11**, 211 (1973).
8. J. S. Langer and H. Muller-Krumbhaar, Acta Metall. **26**, 1681 (1978).
9. G. P. Ivantsov, Dokl. Akad. Nauk SSSR **58**, 567 (1947).
10. D. A. Kessler, J. Koplik and H. Levine, Adv. in Phys. **37(2)**, 255 (1988).
11. G. J. Fix, in Free Boundary Problems: Theory and Application, Vol. II, edited by A. Fasano and M. Primicerio, (Piman, Boston, 1983) pg. 580.
12. J. B. Collins and H. Levine, Phys. Rev. B **31**, 6119 (1985).
13. R. Kobayashi, Physica D **63**, 410 (1993).
14. B. T. Murray, A. A. Wheeler and M. E. Glicksman, J. Cryst. Growt **47**, 386 (1995).
15. J. A. Sethian and J. Strain, J. Comp. Phys. **18**, 2313 (1992).
16. R. Almgren, J. Comp. Phys. **106**, 337 (1993).
17. A. R. Roosen and J. E. Taylor, J. Comp. Phys. **114**, 113 (1994).
18. A. Karma and W. J. Rappel, Phys. Rev. E **53**, 3017 (1996); **60(4)**, 3614 (1999); **57(4)**, 4323 (1998).
19. C. Beckermann, H. J. Diepers, I. Steinbach, A. Karma and X. Tong, J. Comp. Phys. **154**, 468 (1999).
20. J. H. Jeong, N. Goldenfeld and J. A. Dantzig, Phys. Rev. E **64**:041602 (2001).
21. http://www.featflow.de
22. C. F. Lange, F. Durst and M. Breuer, Int. J. of Heat and Mass Transfer **41**, 3409 (1998).
23. D. J. Tritton, J. Fluid Mechanics **6**, 547 (1959).
24. B. Huner and R. G. Hussey, Physics of Fluids **20(8)**, 1211 (1977).